Dynamic control of Casimir forces on a nanoflake in a liquid through a tunable graphene layer

Haruko Toyama ●,[*] Taro Ikeda ●, and Hideo Iizuka ●[†]

Toyota Central R&D Labs., Inc., Nagakute, Aichi 480-1192, Japan

The levitation of a metallic nanoflake has been experimentally demonstrated in liquid by manipulating the Casimir force with a proper choice of materials, and as a step further, dynamic control of the Casimir force acting on a nanoflake is of great importance. We show that the Casimir force acting on a nanoflake in ethanol can be dynamically controlled by adjusting the chemical potential of a graphene layer sandwiched by the Teflon film and the SiO_2 substrate at a distance away from the nanoflake, where the nanoflake can consist of either monolayer graphene or solid material. We develop a harmonic oscillator model that captures the dynamics of the nanoflake observed in numerical calculations. The time constant in the dynamics for a graphene nanoflake is 3 to 6 times longer than that for a gold nanoflake. The upper limit of the zero-force position of the nanoflake is discussed. Our scheme, through the use of the tunable graphene layer, significantly extends the degrees of freedom for dynamic control of nanoflakes in liquid.

I. INTRODUCTION

Casimir forces between bodies in close proximity arise from electromagnetic fluctuations [1–4], and have been extensively explored both in [5–9] and out of [10–13] thermal equilibrium, elucidating the dependencies of geometries [14–19] and materials [20–23], and finding opportunities toward nanomechanical systems [24–27]. Casimir forces out of thermal equilibrium in vacuum can be repulsive [28,29], but they may need sophisticated experimental setups for the control of the temperature. Casimir forces in thermal equilibrium in vacuum are attractive for reciprocal materials [30] while they can be repulsive through the use of nonreciprocal materials such as Weyl semimetals [31–33], indium antimonide [34], and Chern insulators [35,36]. On the other hand, in liquid, repulsive Casimir forces can be generated in proper choices of widely used material bodies. Repulsive Casimir forces were experimentally demonstrated with a combination of gold, bromobenzene, and silica [37].

Recently, the stable zero Casimir forces have been experimentally demonstrated in a system consisting of a gold nanoflake in ethanol at a distance away from the Teflon film backed by the gold substrate [38]. Since then, significant efforts have been devoted to the control of a gold nanoflake, including the use of vanadium dioxide [39], indium tin oxide [40], and external laser illumination [41]. Active control of a two-dimensional nanoflake such as graphene is expected to provide intriguing phenomena for biological and chemical sensing and analyses [42–44]. However, the dynamics of a two-dimensional nanoflake in liquid has not been investigated.

In this paper, we show that the position of a monolayer graphene nanoflake in ethanol can be dynamically controlled by adjusting the chemical potential of a graphene layer sandwiched by the Teflon film and the SiO_2 substrate at a distance away from the nanoflake. Our control scheme is general and operates when the nanoflake consists of various solid materials. The rest of the paper is organized as follows. In Sec. II, we present the geometry of our system and the formalism for investigating the Casimir force, gravity, buoyancy, and fluid resistance acting on the nanoflake. In Sec. III, we present numerical results for both the static and dynamic cases. In addition, we develop a harmonic oscillator model that captures the dynamics of the nanoflake observed in numerical results. Our results reveal that the time constant in the dynamics for the graphene nanoflake is 3 to 6 times longer than that for a nanoflake consisting of solid materials such as gold. The upper limit of the zero-force position of the nanoflake is discussed. The paper is then concluded in Sec. IV.

II. GEOMETRY AND FORMALISM

A. Geometry

We consider a system consisting of a circular monolayer graphene nanoflake in ethanol at a distance away from the Teflon film backed by the semi-infinite SiO_2 substrate, where a tunable monolayer graphene sheet is inserted between the Teflon film and the semi-infinite SiO_2 substrate, as shown in Figs. 1(a) and 1(b). The chemical potential of the circular monolayer graphene nanoflake in ethanol is fixed, and referred to as the graphene nanoflake. We assume that the chemical potential of the tunable monolayer graphene sheet inserted between the film and the substrate is varied by applying a bias voltage, and is referred to as the tunable graphene. We regard our system as a two-body system; the graphene nanoflake for body 1 and the Teflon film/tunable graphene/semi-infinite SiO_2 substrate for body 2. The two bodies are separated by the ethanol gap. We use the coordinate system where the bottom

————————

*haruko.toyama.zd@mosk.tytlabs.co.jp
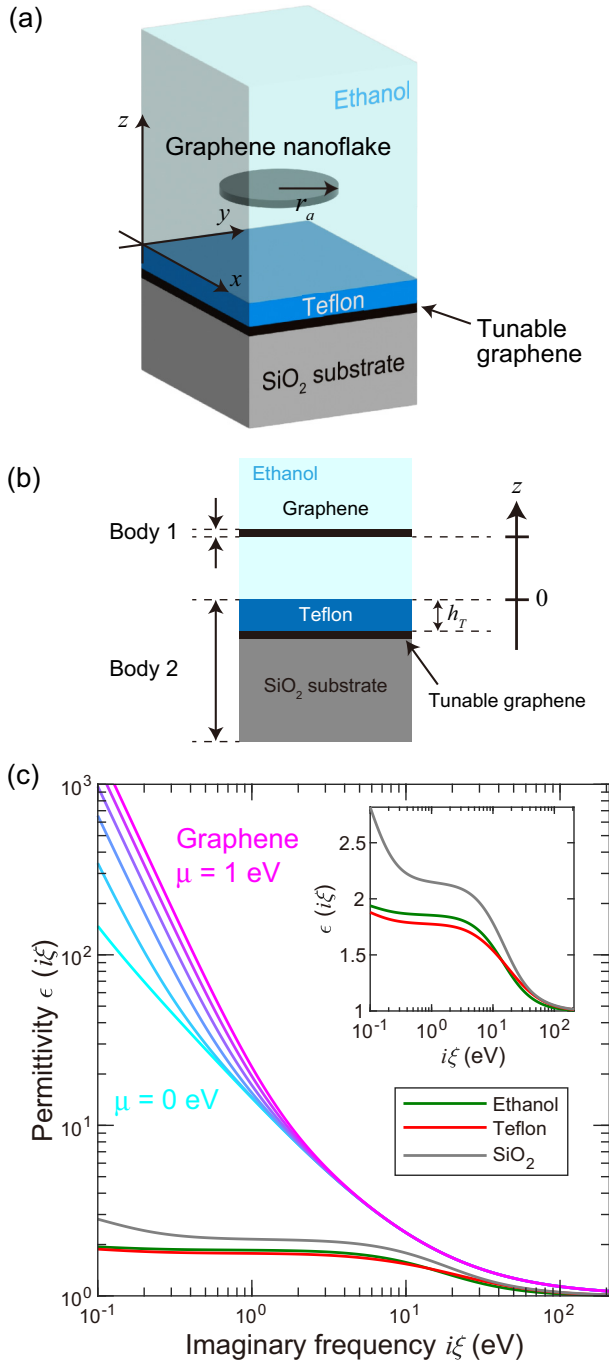
†hiizuka@mosk.tytlabs.co.jp

FIG. 1. (a) Perspective view and (b) cross section of a system consisting of a monolayer graphene nanoflake (body 1) in ethanol at a distance away from the Teflon film/tunable graphene/semi-infinite SiO$_2$ substrate (body 2). (c) Permittivities of ethanol (green), Teflon (red), SiO$_2$ (gray), and monolayer graphene (from cyan to magenta) as a function of imaginary frequency $i\xi$. The chemical potential of the tunable graphene is varied from 0 to 1 eV. The inset is the enlarged view of the permittivities in linear scale for ethanol, Teflon, and SiO$_2$.

surface of the nanoflake is positioned at z with respect to the top surface of the Teflon film. We assume that the system is in equilibrium with temperature T.

The Casimir force acting on the graphene nanoflake (body 1) can be vanished by balancing the attractive and repulsive force components. The attractive force component arises when body 2 consists of the tunable graphene and/or the semi-infinite SiO$_2$ substrate without the Teflon film. On the other hand, the repulsive force component arises when body 2 consists of the Teflon film backed by the semi-infinite ethanol region. The detailed discussion on the force components can be found in Sec. S1 in the Supplemental Material [45]. We note that the system is stable; i.e., when the graphene nanoflake moves close to (away from) body 2, the repulsive (attractive) force is generated on the graphene nanoflake and then moves back to the stable zero-force position.

The position of body 1 for the zero force can be adjusted by two parameters in body 2; one is the thickness h_T of the Teflon film. The other is the chemical potential μ of the tunable graphene, which can be adjusted via a bias voltage. They allow static and dynamic control for the position, respectively.

B. Formalism

We assume that the radius r_a of the graphene nanoflake is much larger than the ethanol gap distance. The Casimir force in thermal equilibrium acting on the graphene nanoflake at position z is calculated by the Wick rotation approach [2],

$$F_{\text{Casimir}}(z) = -A \int_0^\infty \frac{k_\parallel dk_\parallel}{2\pi} \sum_{j=p,s} 2k_B T$$

$$\times \sum_{n=0}^{\infty'} q_{0,n} \frac{\tilde{R}_1^j(i\xi_n, k_\parallel)\tilde{R}_2^j(i\xi_n, k_\parallel)e^{-2q_{0,n}z}}{1 - \tilde{R}_1^j(i\xi_n, k_\parallel)\tilde{R}_2^j(i\xi_n, k_\parallel)e^{-2q_{0,n}z}},$$

(1)

where $A = \pi r_a^2$ is the area of the flake, $k_\parallel$ is the wave-vector component parallel to the surfaces of the bodies, k_B is the Boltzmann constant, $q_{0,n} = \sqrt{\varepsilon_{\text{EtOH}}(i\xi_n)(\frac{\xi_n}{c})^2 + k_\parallel^2}$ is the wave-vector component normal to the surfaces of the bodies, $\xi_n = \frac{2\pi n k_B T}{\hbar}$ is the nth pole in the imaginary frequency axis, c is the speed of light, and $\hbar$ is the reduced Planck constant. $\tilde{R}_1^j$ and $\tilde{R}_2^j$ are the Fresnel reflection coefficients at the interfaces for body 1 (graphene flake) backed by the semi-infinite region of ethanol and body 2 (Teflon film/tunable graphene/semi-infinite SiO$_2$ substrate), respectively, from the ethanol gap region for $j = s$ or p polarization. The prime on the summation represents that the $n = 0$ term is divided by 2. The attractive force is negative in Eq. (1). We assume lossless ethanol with the permittivity in the imaginary frequency axis given by [46]

$$\varepsilon_{\text{EtOH}}(i\xi) = 1 + \sum_j \frac{\omega_{p,j}^2}{\omega_j^2 + \xi^2}, \tag{2}$$

where the parameters in Eq. (2) are presented in Table I. Note that in Refs. [37,38], experimental results of Casimir forces are accurately estimated by using the form of Eq. (2) for lossless liquid. The optical conductivity of a single layer graphene, including the Drude (intraband) and the interband contributions, can be tuned by the chemical potential μ, and

TABLE I. Parameters of the permittivity of Eq. (2) for ethanol taken from Ref. [46].

j	$\omega_{p,j}$ (eV)	ω_j (eV)
1	1.58×10^{-3}	1.62×10^{-3}
2	5.50×10^{-3}	4.32×10^{-3}
3	4.19×10^{-2}	1.12×10^{-1}
4	2.44×10^{0}	6.87×10^{0}
5	9.80×10^{0}	1.52×10^{1}
6	7.71×10^{0}	1.56×10^{1}
7	1.17×10^{1}	4.38×10^{1}

TABLE II. Parameters of the permittivity of Eq. (5) for Au taken from Ref. [53].

j	$\omega_{p,j}$ (eV)	ω_j (eV)	γ_j (eV)
1	8.7663×10^{0}	0.0000×10^{0}	3.9299×10^{-2}
2	1.4869×10^{0}	2.7260×10^{0}	3.2740×10^{-1}
3	2.4205×10^{0}	3.1091×10^{0}	6.0660×10^{-1}
4	4.7921×10^{0}	3.9415×10^{0}	1.3318×10^{0}
5	5.0611×10^{0}	5.2526×10^{0}	2.3931×10^{0}
6	7.3956×10^{0}	7.9749×10^{0}	3.7913×10^{0}
7	6.8464×10^{0}	1.0465×10^{1}	4.9667×10^{0}
8	1.0345×10^{1}	1.4180×10^{1}	7.8967×10^{0}
9	1.3330×10^{1}	2.1207×10^{1}	6.2030×10^{0}
10	1.0279×10^{1}	3.0090×10^{1}	6.9297×10^{0}
11	2.6196×10^{1}	4.2903×10^{1}	4.3564×10^{1}

is given by [47]

$$\sigma(i\xi) = \frac{2e^2 k_B T}{\pi \hbar^2 (\xi + \Gamma)} \ln \left[2\cosh\left(\frac{\mu}{2k_B T}\right) \right]$$
$$+ \frac{e^2}{4\hbar} \left\{ G\left(\frac{i\hbar\xi}{2}\right) + \frac{4\hbar\xi}{\pi} \int_0^\infty \frac{G(\zeta) - G(i\hbar\xi/2)}{\hbar^2\xi^2 + 4\zeta^2} d\zeta \right\},$$
(3)

where $G(\zeta) = \sinh(\zeta/k_B T)/\{\cosh(\mu/k_B T) + \cosh(\zeta/k_B T)\}$, e is the charge of an electron, and Γ is the damping rate of graphene. One can check $G(i\hbar\xi_n/2) = 0$. Equation (3) is valid for estimating Casimir forces in the range of the gap distance we consider throughout the paper [48]. When the gap distance is a few nanometers or less, the optical conductivity obtained from first-principle calculations [49] can estimate even more accurate forces. The permittivity of graphene can be expressed by

$$\varepsilon(i\xi) = 1 + \frac{\sigma(i\xi)}{\xi h_{gr} \varepsilon_0},$$
(4)

where h_{gr} is the thickness of graphene and ε_0 is the free space permittivity [50]. Here we select $h_{gr} = 0.335$ nm, which is the value of the layer distance of AB-stacked bilayer graphene [51]. The permittivities of solid materials in the real frequency axis are approximated by the N-pole Lorentz-Drude model:

$$\varepsilon(\omega) = 1 + \sum_{j=1}^{N} \frac{\omega_{p,j}^2}{\omega_j^2 - \omega^2 - i\gamma_j\omega}.$$
(5)

The parameters of various materials are presented in Tables II–V, taken from Refs. [46,52,53]. The permittivity in the imaginary frequency axis is given by $\varepsilon(i\xi) = 1 + \frac{2}{\pi} \int_0^\infty \frac{\omega \mathrm{Im}[\varepsilon(\omega)]}{\omega^2 + \xi^2} d\omega$ [46,54]. Material properties enter in terms of reflection matrices in Eq. (1). The reflection coefficients for s and p polarizations are presented in Sec. S2 in the Supplemental Material [45].

In the static case, the total force $F_{static}(z)$ acting on body 1 is given by

$$F_{static}(z, \mu) = F_{Casimir}(z, \mu) - mg + \rho V g,$$
(6)

where m and V are the mass and the volume of body 1, respectively. In the right-hand side of Eq. (6), the first term is the Casimir force of Eq. (1), the second term is the gravity with g being the gravitational acceleration, and the third term is the buoyancy with ρ being the density of ethanol, acting on

body 1. The stable zero-force position z_0 of body 1 is defined by $F_{static}(z_0) = 0$.

In the dynamic case, the equation of motion in our system is given by

$$m\frac{d^2 z}{dt^2} = F_{static}[z, \mu(t)] - \frac{3\pi \eta r_a^4}{2z^3} \frac{dz}{dt},$$
(7)

where the first term is the force of Eq. (6) and the second term is the fluid resistance acting on body 1 with the ethanol viscosity of η. In Eq. (7), we have assumed that the optical conductivity of graphene responds fast enough to be set by the chemical potential. A detailed discussion on the model of the fluid resistance is found in Sec. S3 in the Supplemental Material [45].

For numerical investigations, throughout the paper, we use a circular area of $A = \pi r_a^2 = 1$ μm^2 and a chemical potential of 0 eV for the graphene nanoflake. The chemical potential of the tunable graphene is varied from 0 to 1 eV. A damping rate of $\Gamma = 10^{13}$ rad/s is used for graphene in both bodies 1 and 2. The Teflon film has a thickness of $h_T = 20$ nm unless otherwise mentioned. A temperature of $T = 300$ K is selected.

III. RESULTS

Based on the formalism above, we numerically investigate the Casimir forces in the system of Fig. 1. In Sec. III A, we show that there exists the zero-force position of the graphene nanoflake in our system, which can be tuned by adjusting the

TABLE III. Parameters of the permittivity of Eq. (5) for Teflon taken from Ref. [46]. The lossless case with $\gamma_j = 0$ is assumed.

j	$\omega_{p,j}$ (eV)	ω_j (eV)
1	2.89×10^{-5}	3.00×10^{-4}
2	1.03×10^{-3}	7.60×10^{-3}
3	2.08×10^{-2}	5.57×10^{-2}
4	4.22×10^{-2}	1.26×10^{-1}
5	2.96×10^{0}	6.71×10^{0}
6	1.23×10^{1}	1.86×10^{1}
7	1.37×10^{1}	4.21×10^{1}
8	1.52×10^{1}	7.76×10^{1}

TABLE IV. Parameters of the permittivity of Eq. (5) for SiO$_2$ taken from Ref. [46]. The lossless case with $\gamma_j = 0$ is assumed.

j	$\omega_{p,j}$ (eV)	ω_j (eV)
1	3.64×10^{-2}	4.11×10^{-2}
2	5.05×10^{-2}	1.12×10^{-1}
3	7.23×10^{-2}	1.12×10^{-1}
4	6.96×10^{-2}	1.11×10^{-1}
5	3.25×10^{0}	1.45×10^{1}
6	1.54×10^{1}	1.70×10^{1}
7	3.79×10^{0}	8.14×10^{0}
8	2.15×10^{1}	9.16×10^{1}

chemical potential of the tunable graphene. In Sec. III B, we show that the graphene nanoflake can be dynamically moved, and the time constants are discussed comparing with the cases of various metallic flakes. In addition, we develop an analytic model that captures the dynamic behaviors observed in numerical results. In Sec. III C, we discuss the behaviors of the zero-force position and the time constant for various material cases, including the upper limit of the zero-force position.

A. Static characteristic

We firstly examine the permittivities of material bodies in the imaginary frequency axis, as shown in Fig. 1(c). We see that the permittivity of graphene can be tuned by adjusting the chemical potential. In addition, the condition of the repulsive force for permittivities [37] is satisfied in the three materials of Teflon, ethanol, and graphene, i.e., $\varepsilon_{\text{Teflon}}(i\xi) < \varepsilon_{\text{EtOH}}(i\xi) < \varepsilon_{\text{graphene}}(i\xi)$, in the range of $i\xi$ for the dominant contribution to the Casimir force.

Using Eq. (1), we numerically investigate the Casimir forces with variation of position z of body 1 for various chemical potentials μ of the tunable graphene, as shown in Fig. 2(a). The total force in the vertical axis includes the contributions from the gravity and buoyancy being 7.5×10^{-18} and 2.6×10^{-18} N, respectively, which are much smaller than the Casimir force. When the position z of body 1 is larger than z_0, the Casimir force is attractive (negative), which dominantly arises from the combination of the graphene nanoflake/ethanol/tunable graphene/SiO$_2$. As body 1 gets closer to body 2, i.e., $z < z_0$, the Casimir force becomes repulsive (positive) since the repulsive force component dominantly arising from the combination of graphene nanoflake/ethanol/Teflon is drastically enhanced. Interestingly, the zero-force position is described by a function of the

TABLE V. Parameters of permittivities of Eq. (5) for Ag, Cu, Al, and In taken from Ref. [52]. A single-pole Drude model with $\omega_1 = 0$ is used.

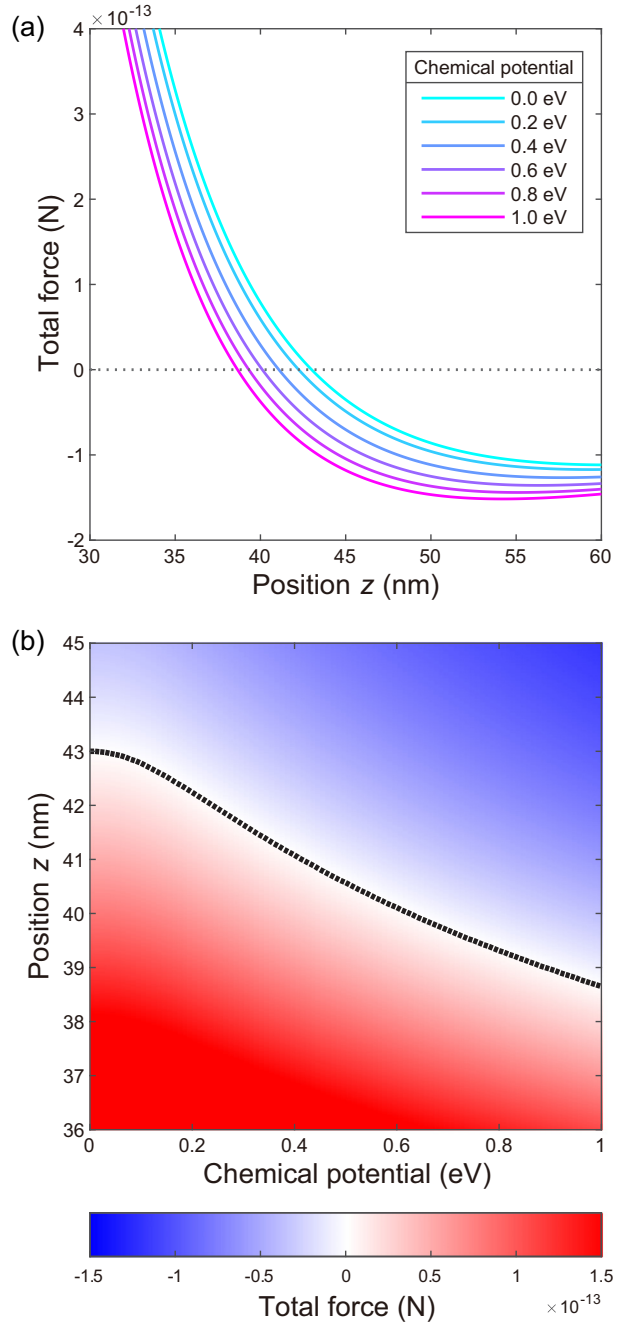|	$\omega_{p,1}$ (eV)	γ_1 (eV)
Ag	9.04	0.02125
Cu	8.76	0.0955
Al	12.04	0.1287
In	12.8	0.46

FIG. 2. (a) Force acting on the nanoflake, including the Casimir force, gravity, and buoyancy, as a function of position z of body 1. The chemical potential of the tunable graphene is varied from 0 to 1 eV. (b) Two-dimensional map of the total force as functions of position z and chemical potential μ. Positive (red) and negative (blue) values represent repulsive and attractive forces, respectively. The black dotted line represents the zero-force position labeled by z_0.

chemical potential $z_0 = z_0(\mu)$, and can be varied from 38.6 to 43.0 nm when μ is adjusted from 1 to 0 eV. In addition, the derivative of each curve around z_0 becomes small as μ decreases from 1 to 0 eV. This implies that each of the attractive and repulsive force components has a small value when the nanoflake at z_0 is away from body 2. The characteristics
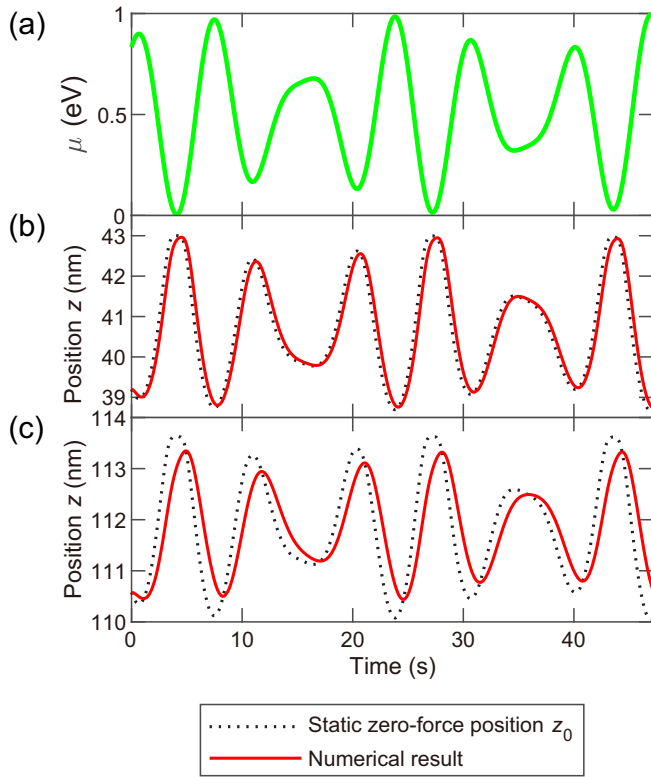
FIG. 3. (a) Time variation of chemical potential μ of the tunable graphene. (b), (c) Position z of the nanoflake dynamically controlled by μ. Black dotted lines represent the zero-force position z_0 in the static case [Eq. (6)]. The red solid lines represent numerically calculated results of position z [Eq. (7)]. The Teflon film has a thickness of $h_T = 20$ nm for (b) or $h_T = 50$ nm for (c).

of z_0 (black dotted line) and the derivative on z (white region around the black dotted line) discussed above are clearly seen in the map as functions of z and μ in Fig. 2(b).

B. Dynamic characteristic

We next investigate the dynamic control of the position of the nanoflake by tuning the chemical potential of the tunable graphene. Here, the chemical potential is varied with respect to μ_c as

$$\mu(t) = \mu_a \sin(\omega_a t) + \mu_b \sin(\omega_b t) + \mu_c. \tag{8}$$

For numerical investigations, we select $\mu_a = 0.33$ eV, $\mu_b = 0.17$ eV, $\omega_a = 0.8$ rad/s, $\omega_b = 1.1$ rad/s, and $\mu_c = 0.5$ eV. The modulation frequencies ω_a and ω_b are sufficiently small so that Eq. (3) is valid. The time response of the chemical potential is shown in Fig. 3(a). The resulting time response of the position of body 1 is numerically obtained by using Eqs. (7) and (8) for each of thicknesses $h_T = 20$ and 50 nm for the Teflon film, and are shown by red solid lines in Figs. 3(b) and 3(c), respectively. The prescribed trajectory, which is the zero-force position $z_0[\mu(t)]$ in the static case, obtained by Eq. (6) is represented by the black dotted line. The temporal dependence of the position of the graphene nanoflake is able to conform to the prescribed trajectory for $h_T = 20$ nm [Fig. 3(b)]. On the other hand, for $h_T = 50$ nm [Fig. 3(c)], the
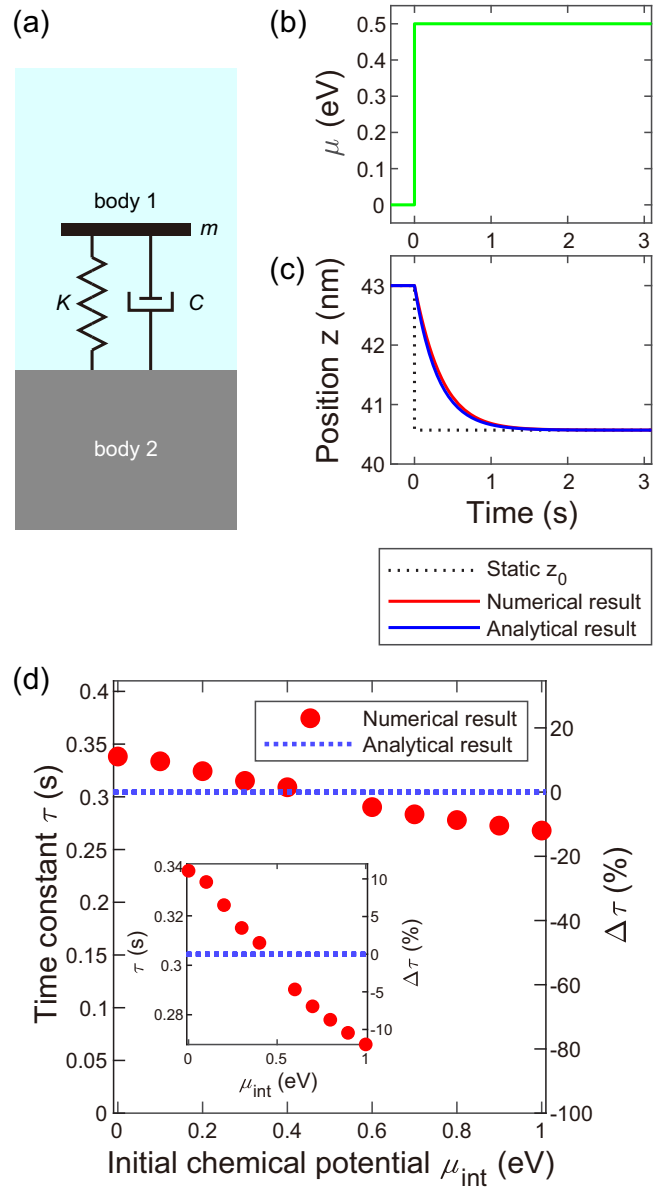

FIG. 4. (a) Harmonic oscillator model for the system of Fig. 1, with m, K, and $C = 3\pi \eta r_a^4 / 2z_{\text{avg}}^3$ being the mass, spring constant, and fluid resistance coefficient. Time variation of (b) chemical potential μ of the tunable graphene and (c) position z of the nanoflake. The red and blue lines in (c) represent position z obtained by numerical and analytical calculations, respectively. The black dotted line represents the static zero-force position z_0. (d) Comparison of time constant τ obtained by numerical (red symbols) and analytical (blue dotted line) calculations. Deviations $\Delta\tau$ of the numerical results with respect to the analytical result are presented by the right axis. The inset is the enlarged view with a range of $\pm 12\%$ for $\Delta\tau$.

resulting time response (red solid line) is delayed from the prescribed trajectory (black dotted line). For understanding the time response behavior above, next we develop a harmonic oscillator model and discuss time constants for various materials for body 1.

The harmonic oscillator model for the system of Fig. 1 consists of the mass, spring, and damper, as shown in Fig. 4(a),

and the equation of motion is given by

$$m\frac{d^2z}{dt^2} + K(z - z_{\text{avg}}) + C\frac{dz}{dt} = 0, \qquad (9)$$

where $z_{\text{avg}} \equiv z_0(\mu_{\text{avg}})$ is the zero-force position with μ_{avg} being the time-averaged $\mu(t)$, e.g., $\mu_{\text{avg}} = \mu_c$ in Eq. (8), which is determined from the static force including the Casimir force, gravity, and buoyancy. We assume that the spring constant K and the fluid resistance coefficient C are constant:

$$K = -\frac{dF_{\text{Casimir}}(z)}{dz}\bigg|_{z=z_{\text{avg}}}, \qquad (10)$$

$$C = \frac{3\pi \eta r_a^4}{2z_{\text{avg}}^3}. \qquad (11)$$

Using Eqs. (10) and (11), Eq. (9) is rewritten as

$$\frac{d^2z}{dt^2} + \omega_r^2(z - z_{\text{avg}}) + 2\zeta\frac{dz}{dt} = 0, \qquad (12)$$

where $\omega_r = \sqrt{K/m}$ is the resonant frequency and $\zeta = C/2m$ is the damping rate. Since $\zeta \gg \omega_r$ in our system, the motion of the nanoflake is in the overdamping oscillation. Thus, the general form of the solutions for an overdamping oscillation is applicable to our system,

$$z = z_{\text{avg}} + a_1 \exp\left[-\left(\zeta - \sqrt{\zeta^2 - \omega_r^2}\right)t\right]$$
$$+ a_2 \exp\left[-\left(\zeta + \sqrt{\zeta^2 - \omega_r^2}\right)t\right], \qquad (13)$$

where a_1 and a_2 are constant coefficients. Considering the condition $\zeta \gg \omega_r$, the third term in the right-hand side of Eq. (13) decays much faster than the second term. Therefore, the time constant is given by

$$\tau = \left(\zeta - \sqrt{\zeta^2 - \omega_r^2}\right)^{-1}. \qquad (14)$$

Before examining the dynamics of the system of Fig. 1 in detail, we validate the analytic model above by observing the time response of the position of the graphene nanoflake in the system of Fig. 1 when the chemical potential of the tunable graphene is changed as the step function:

$$\mu(t) = \begin{cases} \mu_{\text{int}}(t < 0) \\ \mu_{\text{fin}}(t \geqslant 0) \end{cases}. \qquad (15)$$

We first select $\mu_{\text{int}} = 0$ eV and $\mu_{\text{fin}} = 0.5$ eV [Fig. 4(b)]. For $t < 0$, the graphene nanoflake in the system of Fig. 1 stays at the initial position $z_0(\mu_{\text{int}}) = 43.0$ nm. When the chemical potential is changed at $t = 0$, the graphene nanoflake starts to move and approach the position $z_0(\mu_{\text{fin}}) = 40.6$ nm [red line in Fig. 4(c)]. We define time constant τ such that position $z(t = \tau)$ satisfies

$$\left|\frac{z(t = \tau) - z_0(\mu_{\text{fin}})}{z_0(\mu_{\text{int}}) - z_0(\mu_{\text{fin}})}\right| = \frac{1}{e}. \qquad (16)$$

From Eq. (16), a time constant of $\tau = 0.338$ s is obtained for the system of Fig. 1 by solving Eq. (7) [red line in Fig. 4(c)]. Using the analytic model [Fig. 4(a)], the corresponding time response of z is obtained by solving Eq. (9) [blue line in Fig. 4(c)] and the time constant with $z_{\text{avg}} = z_0(\mu_{\text{fin}})$ is calculated to be 0.304 s, which agrees with the
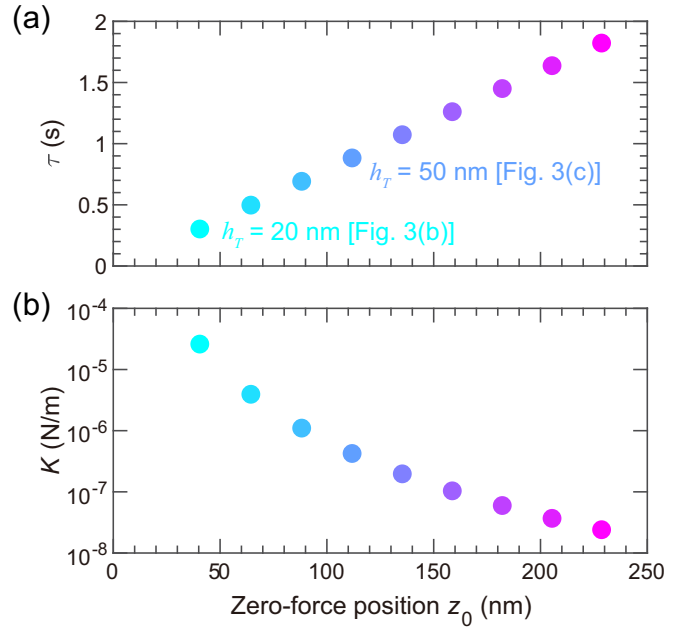

FIG. 5. (a) Time constant τ and (b) spring constant K as a function of zero-force position $z_0(\mu_{\text{fin}} = 0.5$ eV). Thickness h_T of the Teflon film is varied from 20 nm (cyan) to 100 nm (magenta) with a step of 10 nm.

numerical result above. Next, we vary the initial chemical potential μ_{int} from 0 to 1 eV with $\mu_{\text{fin}} = 0.5$ eV fixed, and obtain time constant τ in Fig. 4(d) from the same process. We see that time constant τ using Eq. (7) falls in a range from 0.338 to 0.268 s (symbols). The deviation from the analytical result of $\tau = 0.304$ s (horizontal blue dotted line) is below $\pm 12\%$. Thus, we have verified the validity of the analytic model, i.e., the time constant captures the behavior of the system of Fig. 1.

Based on the harmonic oscillator model above, we calculate time constant τ from Eq. (14), as shown in Fig. 5(a). We have varied thickness h_T of the Teflon film from 20 nm (cyan) to 100 nm (magenta) with a step of 10 nm, and the corresponding zero-force position z_0 is used for the horizontal axis in Figs. 5(a) and 5(b). We observe that τ increases with the increase of z_0. When the Teflon film is $h_T = 20$ nm, which corresponds to Fig. 3(b), the time constant is $\tau = 0.302$ s, which is much smaller than the inverse of modulation frequencies $2\pi/\omega_a = 7.854$ s and $2\pi/\omega_b = 5.672$ s. Therefore, the excellent tractability was observed in Fig. 3(b). On the other hand, for $h_T = 50$ nm, corresponding to Fig. 3(c), the time constant is $\tau = 0.883$ s, and the delay time in the time response is comparable to the time constant in Fig. 3(c). As shown in Fig. 5(b), spring constant K decreases.

The tractability of the nanoflake, which is observed in Fig. 3, can be understood as follows. When μ is selected to be 0.5 eV, the zero-force position z_0 is 40.5 nm for $h_T = 20$ nm, and 111.8 nm for $h_T = 50$ nm (see Sec. S4 in the Supplemental Material [45]). In our system, the Casimir force acting on the graphene nanoflake in the system of Fig. 1 can be decomposed into the attractive force component in the structure with body 2 consisting of the tunable graphene/semi-infinite SiO$_2$ substrate, and the repulsive force

component in the structure with body 2 consisting of the Teflon film for the whole range of μ we consider here (see Sec. S5 in the Supplemental Material [45]). As body 1 goes away from body 2, magnitudes of the repulsive and attractive force components at z_0 decrease, which indicates a smaller spring constant (4.24×10^{-7} N/m) for $h_T = 50$ nm than that (2.60×10^{-5} N/m) for $h_T = 20$ nm. Under the condition of $\omega_r/\zeta \ll 1$, the time constant of Eq. (14) is approximated to be a simpler form of

$$\tau = \left\{ \zeta \left[1 - \sqrt{1 - \left(\frac{\omega_r}{\zeta}\right)^2} \right] \right\}^{-1}$$

$$\approx \left\{ \zeta \left[1 - \left(1 - \frac{1}{2}\left(\frac{\omega_r}{\zeta}\right)^2 \right) \right] \right\}^{-1} = \frac{2\zeta}{\omega_r^2} = \frac{C}{K}. \quad (17)$$

τ should be shorter for larger K as shown in Eq. (17), which suggests better tractability in the case of $h_T = 20$ nm.

We have so far investigated the dynamics of the system of Fig. 1 with body 1 being a graphene nanoflake. Our control scheme through the use of the tunable graphene in body 2 is not limited to a two-dimensional material for body 1; i.e., the position of a nanoflake for other materials is able to be controlled. Here, we investigate five solid materials, which are gold (Au), silver (Ag), copper (Cu), aluminum (Al), and indium (In), for body 1 in the system of Fig. 1, and discuss the dynamics in terms of time constants. We select a thickness of 45 nm for the five solid materials [38]. Figure 6(a) shows the comparison of zero-force positions z_0 in the static state for the five solid materials and graphene with each having three thicknesses $h_T = 20$, 50, and 80 nm for the Teflon film. We see that z_0 of graphene is $1.3-1.5$ times larger than that of the five solid materials for each h_T. For example, in the case of $h_T = 20$ nm (circles), the zero-force positions are 40.5, 29.8, 28.6, 28.5, 29.5, and 29.6 nm for graphene, Au, Ag, Cu, Al, and In, respectively. Spring constant K in the analytic model of Fig. 4(a) is numerically obtained from Eq. (10), and plotted in Fig. 6(b). K for the graphene case is approximately one order smaller than that for the cases of the five solid materials. This comes from the fact that in the graphene case, each magnitude of the decomposed attractive and repulsive components is 2 to 5 times smaller, comparing with the cases of the five solid materials. (A detailed discussion on the decomposition into the attractive and repulsive components is found in Sec. S5 in the Supplemental Material [45].) The corresponding time constants are obtained from Eq. (14) with spring constant K [Eq. (10)] and fluid resistance coefficient C [Eq. (11)] being incorporated, and plotted in Fig. 6(c). As expected from the contrast of K in Fig. 6(b), the time constant for the graphene case is 3 to 6 times longer than that for the cases of the five solid materials.

C. Discussion

We have shown that proper choices of the material and the zero-force position of the nanoflake can provide the time constant over a range of 3 to 6 times, which significantly extends the degrees of freedom for the dynamic control of the nanoflake. For example, a large time constant is benefi-
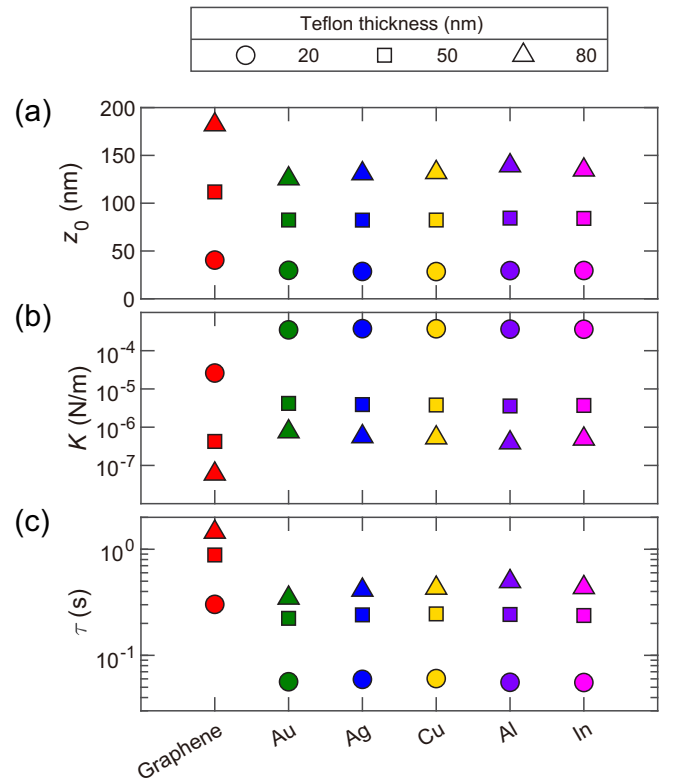

FIG. 6. Comparison of (a) zero-force positions z_0, (b) spring constants K, and (c) time constants τ for the graphene case with those of solid material cases. Circles, squares, and triangles represent the results for thicknesses $h_T = 20$, 50, and 80 nm of the Teflon film, respectively. A chemical potential $\mu = 0.5$ eV is selected for the tunable graphene.

cial when the robustness against noises and disturbances is required for a system. On the other hand, a small time constant is preferred when a prompt response is required.

We emphasize that there exists the upper limit of the zero-force position $z_{0,\mathrm{UL}}$. As thickness h_T of the Teflon film increases, z_0 increases and approaches $z_{0,\mathrm{UL}}$ (see Fig. S2(c) in the Supplemental Material [45]). This behavior of z_0 can be understood as follows. As z_0 goes away from body 2, both of the decomposed attractive and repulsive Casimir force components decrease. When $h_T \to \infty$, the attractive Casimir force component $F_{\mathrm{att}}(z)$ becomes negligibly small and the repulsive Casimir force component $F_{\mathrm{rep}}(z)$ is comparable to gravity mg and buoyancy $\rho V g$, i.e., z_0 is no longer dependent on h_T and μ, and the upper limit $z_{0,\mathrm{UL}}$ satisfies

$$F_{\mathrm{rep}}(z_{0,\mathrm{UL}}) - mg + \rho V g = 0. \quad (18)$$

With $h_T \geqslant 5$ μm, z_0 reaches $z_{0,\mathrm{UL}} = 2310$ nm, which is obtained when body 2 consists of the semi-infinite Teflon substrate. (green dotted line in Fig. S2(c) in the Supplemental Material [45]). Consequently, there exists the upper limit of time constant τ as well.

Though we have used ethanol in our system, other liquids can also be used instead, e.g., cyclopentane, cyclohexane, cycloheptane, cyclo-octane, benzene, fluorobenzene, chlorobenzene, bromobenzene, iodobenzene, toluene, hexane, heptane, octane, dodecane, water, methanol, propanol,

butanol, iodomethane, diiodomethane, tetrachloromethane, glycerol, and styrene (see Sec. S6 in the Supplemental Material [45]). Interestingly, zero-force position z_0 and its upper limit $z_{0,UL}$ are largely varied with a proper choice of liquid, which leads to highly flexible choice of the time constant. We also note that the nanoflake having relatively small permittivity can also be levitated in liquid by the Casimir force. For example, a Teflon nanoflake can be levitated when body 2 consists of the tunable graphene backed by the Teflon substrate (see Sec. S6 in the Supplemental Material [45]). Thus, our scheme allows the controllable levitation of nanoflakes in liquid with highly flexible choices of materials, which is significantly advantageous for applications in biological and chemical sensing and analyses.

IV. CONCLUSIONS

We have investigated the Casimir forces acting on a graphene nanoflake in ethanol at a distance away from the Teflon film backed by the semi-infinite SiO_2 substrate, where a tunable graphene is inserted. Numerical results showed that the position of the nanoflake was dynamically controlled by adjusting the chemical potential of the tunable graphene, including the effects of the gravity, buoyancy, and fluid resistance. We developed a harmonic oscillator model that captured the dynamics of the nanoflake. Numerical and analytical results have revealed that the time constant in the dynamics for the graphene nanoflake is 3 to 6 times longer than that for a nanoflake consisting of solid materials. The upper limit of the zero-force position of the nanoflake was discussed with the corresponding structure. Our scheme through the use of the tunable graphene layer significantly extends the degrees of freedom for dynamic control of nanoflakes in liquid.

[1] H. B. Casimir, Proc. Kon. Ned. Akad. Wet. **51**, 793 (1948).

[2] E. M. Lifshitz and M. Hamermesh, in *Perspectives in Theoretical Physics*, edited by L. P. Pitaevskii (Elsevier, Amsterdam, 1992), p. 329.

[3] A. W. Rodriguez, F. Capasso, and S. G. Johnson, Nat. Photonics **5**, 211 (2011).

[4] T. Gong, M. R. Corrado, A. R. Mahbub, C. Shelden, and J. N. Munday, Nanophotonics **10**, 523 (2021).

[5] S. K. Lamoreaux, Phys. Rev. Lett. **78**, 5 (1997).

[6] G. Bressi, G. Carugno, R. Onofrio, and G. Ruoso, Phys. Rev. Lett. **88**, 041804 (2002).

[7] C. Henkel, K. Joulain, J. P. Mulet, and J. J. Greffet, Phys. Rev. A **69**, 023808 (2004).

[8] R. S. Decca, D. Lopez, E. Fischbach, G. L. Klimchitskaya, D. E. Krause, and V. M. Mostepanenko, Phys. Rev. D **75**, 077101 (2007).

[9] H. Iizuka and S. H. Fan, J. Opt. Soc. Am. B **36**, 2981 (2019).

[10] M. Antezza, L. P. Pitaevskii, S. Stringari, and V. B. Svetovoy, Phys. Rev. Lett. **97**, 223203 (2006).

[11] M. Kruger, T. Emig, and M. Kardar, Phys. Rev. Lett. **106**, 210404 (2011).

[12] K. F. Chen and S. H. Fan, Phys. Rev. Lett. **117**, 267401 (2016).

[13] A. E. R. Lopez, P. M. Poggi, F. C. Lombardo, and V. Giannini, Phys. Rev. A **97**, 042508 (2018).

[14] G. L. Klimchitskaya, U. Mohideen, and V. M. Mostepanenko, Rev. Mod. Phys. **81**, 1827 (2009).

[15] A. W. Rodriguez, D. Woolf, A. P. McCauley, F. Capasso, J. D. Joannopoulos, and S. G. Johnson, Phys. Rev. Lett. **105**, 060401 (2010).

[16] M. F. Dou, F. Lou, M. Bostrom, I. Brevik, and C. Persson, Phys. Rev. B **89**, 201407 (2014).

[17] L. M. Woods, D. A. R. Dalvit, A. Tkatchenko, P. Rodriguez-Lopez, A. W. Rodriguez, and R. Podgornik, Rev. Mod. Phys. **88**, 045003 (2016).

[18] D. A. T. Somers and J. N. Munday, Phys. Rev. A **95**, 022509 (2017).

[19] C. Abbas, B. Guizal, and M. Antezza, Phys. Rev. Lett. **118**, 126101 (2017).

[20] A. Lambrecht and V. N. Marachevsky, Phys. Rev. Lett. **101**, 160403 (2008).

[21] A. W. Rodriguez, A. P. McCauley, D. Woolf, F. Capasso, J. D. Joannopoulos, and S. G. Johnson, Phys. Rev. Lett. **104**, 160402 (2010).

[22] M. Levin, A. P. McCauley, A. W. Rodriguez, M. T. H. Reid, and S. G. Johnson, Phys. Rev. Lett. **105**, 090403 (2010).

[23] J. L. Garrett, D. A. T. Somers, and J. N. Munday, Phys. Rev. Lett. **120**, 040401 (2018).

[24] H. B. Chan, V. A. Aksyuk, R. N. Kleiman, D. J. Bishop, and F. Capasso, Science **291**, 1941 (2001).

[25] L. Tang, M. Wang, C. Y. Ng, M. Nikolic, C. T. Chan, A. W. Rodriguez, and H. B. Chan, Nat. Photonics **11**, 97 (2017).

[26] H. Iizuka and S. H. Fan, Appl. Phys. Lett. **118**, 144001 (2021).

[27] H. Iizuka and S. H. Fan, J. Quant. Spectrosc. Radiat. Transfer **289**, 108281 (2022).

[28] R. Messina and M. Antezza, Phys. Rev. A **84**, 042102 (2011).

[29] H. Iizuka and S. H. Fan, J. Opt. Soc. Am. B **38**, 151 (2021).

[30] S. J. Rahi and S. Zaheer, Phys. Rev. Lett. **104**, 070405 (2010).

[31] J. H. Wilson, A. A. Allocca, and V. Galitski, Phys. Rev. B **91**, 235115 (2015).

[32] Z. Li and C. Khandekar, Phys. Rev. Appl. **16**, 044047 (2021).

[33] J. N. Rong, L. Chen, and K. Chang, Chin. Phys. Lett. **38**, 084501 (2021).

[34] S. Fuchs, F. Lindel, R. V. Krems, G. W. Hanson, M. Antezza, and S. Y. Buhmann, Phys. Rev. A **96**, 062505 (2017).

[35] P. Rodriguez-Lopez and A. G. Grushin, Phys. Rev. Lett. **112**, 056804 (2014).

[36] P. Rodriguez-Lopez, D. N. Le, M. J. Calderón, E. Bascones, and L. M. Woods, 2D Mater. **10**, 014006 (2023).

[37] J. N. Munday, F. Capasso, and V. A. Parsegian, Nature (London) **457**, 170 (2009).

[38] R. K. Zhao, L. Li, S. Yang, W. Bao, Y. Xia, P. Ashby, Y. Wang, and X. Zhang, Science **364**, 984 (2019).

[39] L. X. Ge, X. Shi, Z. J. Xu, and K. Gong, Phys. Rev. B **101**, 104107 (2020).

[40] L. X. Ge, X. Shi, L. Liu, and K. Gong, Phys. Rev. B **102**, 075428 (2020).

[41] B. Munkhbat, A. Canales, B. Kucukoz, D. G. Baranov, and T. O. Shegai, Nature (London) **597**, 214 (2021).

[42] F. Schedin, A. K. Geim, S. V. Morozov, E. W. Hill, P. Blake, M. I. Katsnelson, and K. S. Novoselov, Nat. Mater. **6**, 652 (2007).

[43] Y. Ohno, K. Maehashi, Y. Yamashiro, and K. Matsumoto, Nano Lett. **9**, 3318 (2009).

[44] N. Mohanty and V. Berry, Nano Lett. **8**, 4469 (2008).

[45] See Supplemental Material at http://link.aps.org/supplemental/10.1103/PhysRevB.108.245402 for the Casimir force components, the reflection coefficients, the model of the fluid resistance, the effects of the Teflon thickness, the effects of the Casimir force components on the dynamics, and the Casimir force with various materials, which also includes Refs. [55,56].

[46] P. J. van Zwol and G. Palasantzas, Phys. Rev. A **81**, 062502 (2010).

[47] L. A. Falkovsky, J. Phys.: Conf. Ser. **129**, 012004 (2008)

[48] Y. Jeyar, K. Austry, M. Luo, B. Guizal, H. Chan, and M. Antezza, Phys. Rev. B **108**, 115412 (2023).

[49] Y. Y. Wang, Z. H. Ni, L. Liu, Y. H. Liu, C. X. Cong, T. Yu, X. J. Wang, D. Z. Shen, and Z. X. Shen, ACS Nano **4**, 4074 (2010).

[50] A. Vakil and N. Engheta, Science **332**, 1291 (2011).

[51] Y. Baskin and L. Meyer, Phys. Rev. **100**, 544 (1955).

[52] E. J. Zeman and G. C. Schatz, J. Phys. Chem. **91**, 634 (1987).

[53] Y. Luo, R. K. Zhao, and J. B. Pendry, Proc. Natl. Acad. Sci. USA **111**, 18422 (2014).

[54] G. Bimonte, Phys. Rev. A **81**, 062501 (2010).

[55] R. Messina and P. Ben-Abdallah, Sci. Rep. **3**, 1383 (2013).

[56] O. Pinkus and B. Sternlicht, *Theory of Hydrodynamic Lubrication* (McGraw-Hill, New York, 1961).